Check for updates

Eect of acid corrosion on physico-mechanical parameters and energy dissipation of granite

Jimiao Zhang[1], Bao Zhang[1,2]*, Yupeng Shen[2]* and Tuo Yang[2]

[1]CHN Energy, Technology and Economics Research Institute, Beijing, China, [2]School of Energy and Mining Engineering, China University of Mining and Technology, Beijing, China

In deep underground engineering, it is inevitable that portions of the rock mass will be subjected to the erosion and chemical corrosion of infiltrating water. A comprehensive study of the physical, mechanical, and energetic properties of rocks after hydrochemical corrosion is crucial for ensuring the stability of the rock mass. The novelty of this research lies in the detailed investigation of the macroscopic and microscopic morphologies of rocks exposed to various corrosive solutions, as well as the changes in various physical and mechanical parameters. Utilizing the weighting method, a scientific comprehensive evaluation system for deep rocks after hydrochemical corrosion has been established. The results indicate a pronounced sensitivity of the macroscopic and microscopic morphologies to pH values. The longitudinal wave velocity of the corroded rock decreases obviously, with the maximum decrease being 13.46%. As the pH value decreases (from 7 to 3), the compressive strength, elastic modulus, cohesion, and internal friction angle of the rocks all decrease significantly. The acidity of the solution significantly aects the changes in the three types of strain energy of the rocks, with higher acidity leading to weaker energy storage capability. Among the factors influencing the characteristics of strain energy variation in rocks, confining pressure has a higher priority than pH value. This study precisely evaluates the impact of hydrochemical corrosion on rock damage using a percentage-based scoring system, and found that granite's score dropped from 81 to 16. The research findings provide valuable insights for the evaluation of rock mass stability under hydrochemical corrosion conditions.

KEYWORDS

geological disaster, deep rock mass, hydrochemical corrosion, macro and micro morphology, mechanical properties, evaluation system

1 Introduction

In the realm of geotechnical engineering, rocks, as the fundamental building blocks of rock mass structures, possess physical, mechanical, and energetic properties that are paramount to the safety and stability of engineered structures (Zhao et al., 2024; Fang et al., 2024; Zhou et al., 2019; Wang et al., 2018; Hao et al., 2022a). Nevertheless, in both natural environments and engineering practices, rocks are inevitably subjected to the corrosive eects of various chemical solutions. For instance, the reaction between impure water in underground coal mines and pyrite, as well as other sulfur-bearing minerals within coal seams (Deng et al., 2024), significantly elevates the concentration of acidic ions in mine water, rendering the surrounding rock in tunnels and old goaf areas

particularly susceptible to acid mine drainage erosion. In actual geothermal exploitation projects, employing chemical corrosion solutions to enhance the permeability of thermal reservoirs can adversely impact the mechanical properties of surrounding rocks and reduce geothermal energy extraction eiciency (Ceglia et al., 2020). Furthermore, during the exploitation of underground mineral resources in oshore regions, acidic ions from seawater infiltrate into mine groundwater, markedly compromising the stability of surrounding rocks (Yang et al., 2019). Chemical corrosion alters the physicochemical properties of rocks, notably influencing their mechanical and energetic performance, thereby posing a latent threat to the long-term stability and safety of geotechnical engineering structures (Wang et al., 2023; Fu et al., 2024; Ren et al., 2024). Consequently, a profound investigation into the eects of chemical solution corrosion on the mechanical and energetic properties of rocks holds significant theoretical value and practical implications.

The investigation into the eects of chemical corrosion on rocks is a pivotal field within the broader discipline. Contemporary rock mechanics theories assert that the influence of chemical solutions on rock mechanics cannot be solely explained by the principle of eective stress (Anderson and Grew, 1977; Atkinson and Meredith, 1981). Consequently, experimental research methodologies have gained widespread acceptance in this area. The majority of studies have focused on the static mechanical implications of chemical solution corrosion on rocks. For instance, Fang et al. (2018) observed that rocks with lower porosity were more prone to biconical failure after treatment with acidic solutions, while smaller rock pores resulted in an increase in transgranular cracks. Lin et al. (2019), utilizing nuclear magnetic resonance (NMR) technology, discovered that chemical corrosion led to an expansion of rock porosity, broadening of the T_2 spectrum, and a more intricate pore structure as the fractal dimension increased. Gong et al. (2021) analyzed the influence of pre-cracking patterns and chemical solutions on rock elastic properties and compressive strength, discussing the constraining eect of chemical corrosion on rock fracture modes. Wu et al. (2021), employing acoustic emission (AE) technology, analyzed distortions in the failure behavior of corroded rocks and identified several failure modes based on final failure patterns and points. Chen et al. (2023) found that as solution acidity increased, both AE energy and counts decreased to varying degrees, with the AE process divisible into stable, active, and sharply progressing stages. Pan et al. (2024), through mechanical testing of chemically corroded rocks, analyzed the eects of confining pressure on rock damage and the brittle-ductile transition, discussing the laws governing the influence of chemical corrosion on rock physical-mechanical behavior. Concurrently, some scholars have also explored the dynamic mechanical eects of chemical solution corrosion on rocks. Xue et al. (2022) discovered that the influence of pH on rock dynamic strength followed a normal distribution, with acidic and alkaline environments significantly impacting rocks while neutral environments had minimal eects. Zhou and Yu (2022), utilizing Split Hopkinson Pressure Bar (SHPB) tests, investigated the dynamic mechanical properties and energy evolution laws of chemically corroded granite, analyzing the chemical reaction process and corrosion mechanisms through X-ray diraction (XRD) and scanning electron microscopy (SEM).

FIGURE 1
Mineral composition of granite.
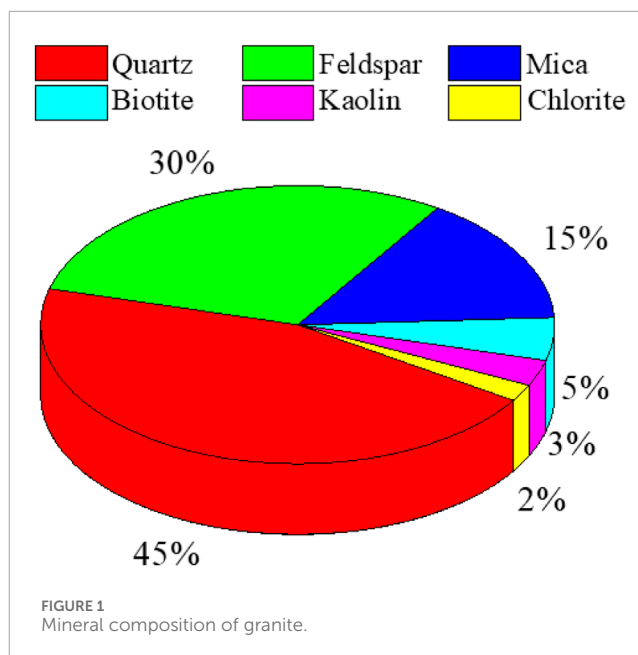
The aforementioned study focusing on the eects of solution corrosion on rocks primarily emphasizes their physical-mechanical properties. Given that the evolution of rock damage is accompanied by the absorption, storage, and release of strain energy, investigating the influence of chemical solution corrosion on rock strain energy becomes a worthy endeavor. Furthermore, the manifestation of chemical corrosion on rocks encompasses alterations in multiple parameters. Current research in this field still lacks a comprehensive evaluation framework for chemically corroded rocks. Merely analyzing the impact of various corrosive conditions on specific parameters is inadequate. It is imperative to integrate changes across several key parameters and establish a comprehensive evaluation system that encapsulates the eects of chemical solution corrosion on rocks.

2 Experimental method

The rock samples utilized in this experiment were sourced from the underground granite deposits of a mine in Shandong Province, specifically from the −1,000 to −1,050 m stratigraphic interval. The rock samples exhibited a grayish-black hue, and the primary mineral constituents of the granite studied were quartz, feldspar, and mica, with respective percentages of 45%, 30%, and 15% (Figure 1).

Based on the laboratory analysis of water samples collected from the site, the primary corrosive ions present in the deep fracture water were identified as Cl^-, SO_4^{2-}, and Mg^{2+}. Consequently, solutions were formulated using NaCl, Na_2SO_4, and $MgCl_2$ to mimic these conditions. Following the methodologies outlined by Chen et al. (2022), solutions with pH values of 3, 5, and 7 were prepared. Rocks soaked in distilled water served as the control group, and all four experimental groups were subjected to a soaking duration of 60 days, with three rock specimens per group. Adhering to the
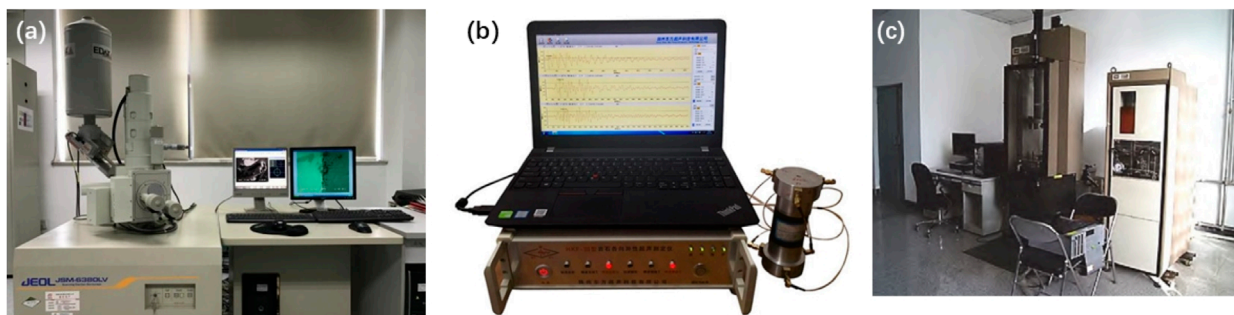
FIGURE 2
The experimental device used in this study **(A)** Scanning Electron Microscope; **(B)** ultrasonic velocity tester; **(C)** MTS815 testing system.

recommendations of the International Society for Rock Mechanics and Rock Engineering (ISRM), the granite was processed into standard cylindrical specimens with dimensions of φ50 mm × 100 mm. Post-corrosion, the micro-morphological characteristics of the rocks were examined using an FEI Quanta 250 FEG Scanning Electron Microscope (Figure 2A). The longitudinal wave velocities of each group of rocks were measured using an HKF-III ultrasonic velocity tester (Figure 2B), and mechanical tests were conducted on the rock specimens using an MTS815 testing system at a loading rate of 1 MPa/s (Figure 2C).

3 Changes in petrophysical parameters

3.1 Macroscopic morphological

Table 1 illustrates the morphological alterations of granite subsequent to hydrochemical corrosion. It is evident from the table that, irrespective of the pH level of the solution, the corrosion traces on the rock sample surfaces progressively intensify with the prolongation of corrosion time, leading to a gradual increase in rock damage. At a pH of 7, the corrosion traces on the rock surface are exceptionally subtle, devoid of discernible pores or fractures. Conversely, at lower pH values, the rock surface exhibits pronounced corrosion marks, accompanied by the emergence of numerous pores. The underlying mechanism responsible for these alterations on the granite surface stems from the chemical reactions between the H^+ ions present in the acidic salt solution and the mineral components, resulting in the formation of microscopic interconnected regions within the rock and contributing to its rough macroscopic morphology. Specifically, the interaction between the H^+ ions in the solution and the mineral constituents triggers these changes. The lower the pH value of the solution, the more pronounced the corrosion traces become on the sample surface, underscoring the insignificance of pure salt ions (at pH 7) in the corrosion process of granite. It is noteworthy that the presence of pre-existing microcracks on the initial rock surface enhances the contact area between the rock minerals and the solution, thereby accelerating the chemical reaction rate and exacerbating the roughness of the granite.

3.2 Micromorphological

Figure 3 presents the microscopic morphologies (magnified 300 times) of granite subjected to various solution treatments. The granite surface treated with distilled water exhibits virtually no corrosion traces, with no discernible changes in the structure between dierent particles. Following hydrochemical corrosion with a solution of pH 7, the granite surface displays mild corrosion, accompanied by a degree of loosening in the structure between particles. When subjected to a pH 5 solution, the granite surface reveals more pronounced corrosion marks, with a heightened level of loosening between particles and the emergence of a few secondary fractures and loose particles. In contrast, the granite exposed to a pH 3 solution undergoes significant corrosion, resulting in a notably loose contact between mineral grains. Numerous pores and loose particles become evident at the mineral cementation interfaces. These observations underscore the influence of solution pH on the degree of corrosion experienced by the samples, which in turn aects their microscopic composition. This highlights the consistency between microstructural alterations and macroscopic morphological changes.

3.3 Longitudinal wave velocity

Figure 4 demonstrates the variation in compressional wave velocity of granite subjected to dierent hydrochemical corrosion treatments. Notably, after treatment with distilled water, the wave velocity of granite exhibits an increasing trend. This phenomenon can be attributed to the fact that the native pores and microcracks within the rock absorb moisture, enhancing the overall compactness of the rock and strengthening its capability to propagate sound waves (Zhao et al., 2020). However, as the soaking duration increases, the increase in wave velocity becomes less pronounced, indicating that the rock has reached a nearly saturated state. Conversely, when the rock is subjected to solutions with varying pH values, a significant decrease in wave velocity is observed. This decrease stems from the chemical reactions between the solution and the minerals within the rock, leading to the degradation of its internal structure. Notably, the most pronounced decrease in wave velocity occurs when the soaking duration is relatively short.

TABLE 1 The change in macroscopic morphology of rock.

PH	0d	9d	15d	60d
3				
5				
7				

4 Mechanical properties of granite

4.1 Uniaxial compression

Figure 5 presents the stress-strain curves of granite subjected to dierent corrosion conditions. It is evident that the lower the pH value, the smaller the uniaxial compressive strength of the rock. (1) Compaction Stage: In this stage, the deformation of the rock is primarily manifested by the compaction of native cracks and pores. However, due to the relatively dense structure of the granite used in this study, the compaction stage in the stress-strain curve is not pronounced. As the pH value increases, the compaction stage transitions from an "approximately convex" shape to an "approximately concave" shape, indicating that hydrochemical corrosion has caused a small amount of irreversible damage within the rock. (2) Elastic stage: The stress-strain curve of granite is approximately straight, in which the rock stores strain energy in an approximately undamaged state (Wang et al., 2016; Zhao et al., 2021). (3) Plastic Stage: During this stage, the curve shifts from a straight line to a convex curve. Microcracks and microvoids within the sample rapidly develop into through-going cracks, leading to the eventual failure of the rock sample (Zhang et al., 2019a; Hao et al., 2022b). The strain of the rock increases with the increase in stress. Notably, the lower the pH value, the more pronounced the yield stage is (indicating a more significant corrosion-softening eect). (4)

Post-Peak Drop Stage: In the naturally dried state, granite undergoes instantaneous brittle fracture upon reaching the peak point, with no discernible post-peak yield stage. However, granite subjected to hydrochemical corrosion exhibits a distinct post-peak yield stage. The hydrochemical corrosion acts as a softening agent on the rock, enabling it to retain a certain level of load-bearing capacity after reaching the peak point instead of undergoing rapid brittle fracture. The lower the pH value, the more pronounced the trend towards ductility from brittleness becomes in the rock.

Equation 1: Poisson's ratio and elastic modulus are crucial parameters that characterize the deformation behavior of rocks. By measuring the slope of the stress-strain curve during the elastic stage, the average elastic modulus of the rock can be obtained (Zhao et al., 2020).

$$\left. \begin{array}{c} E = \dfrac{\sigma_b - \sigma_a}{\varepsilon_{hb} - \varepsilon_{ha}} \\ \mu = \dfrac{\varepsilon_{db} - \varepsilon_{da}}{\varepsilon_{hb} - \varepsilon_{ha}} \end{array} \right\} \tag{1}$$

where, σ_a and σ_b represent the stress values at the starting and ending points of the elastic stage on the stress-strain curve, respectively; ε_{ha} and ε_{hb} are the corresponding axial strains; ε_{da} and ε_{db} are the corresponding radial strains.

Figure 6 illustrates the changes in the elastic modulus and Poisson's ratio of granite after exposure to solutions with dierent pH values. Compared to granite treated with distilled water, the elastic
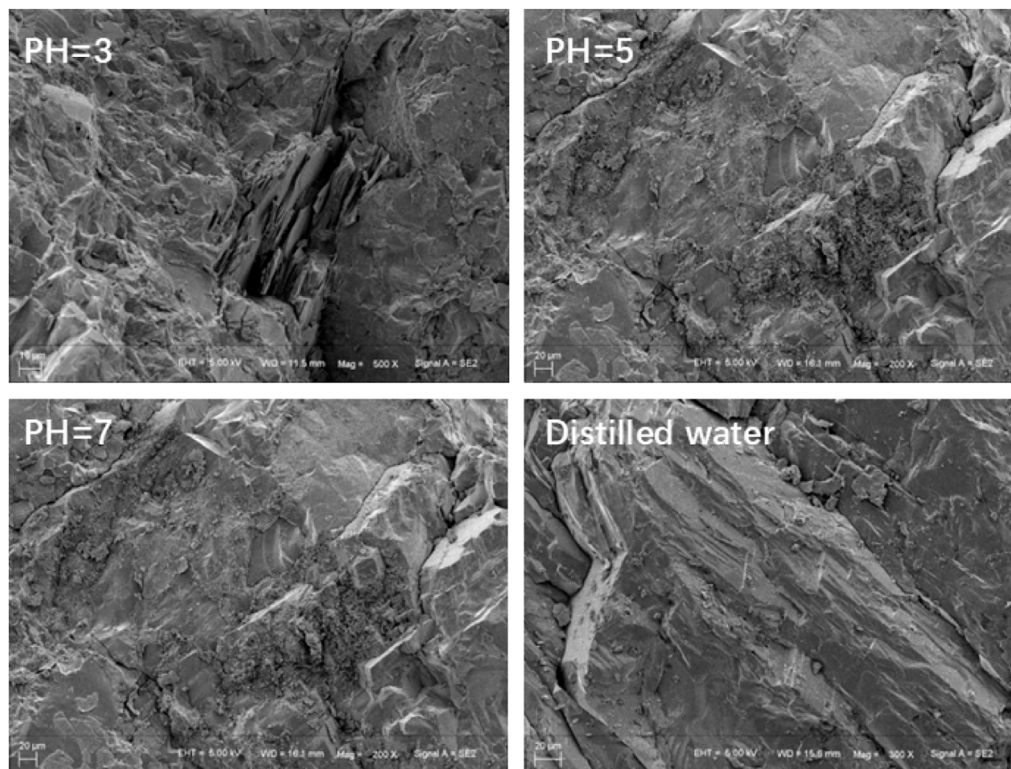
FIGURE 3
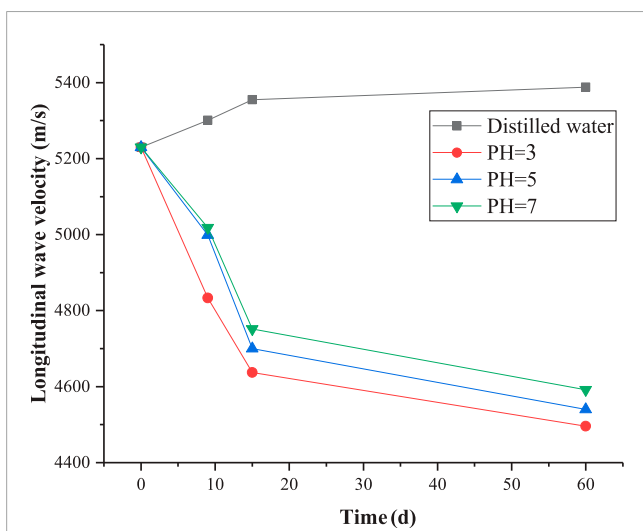Microstructure of granite after corrosion conditions.

FIGURE 4
Changes of p-wave velocity of granite after hydrochemical corrosion.
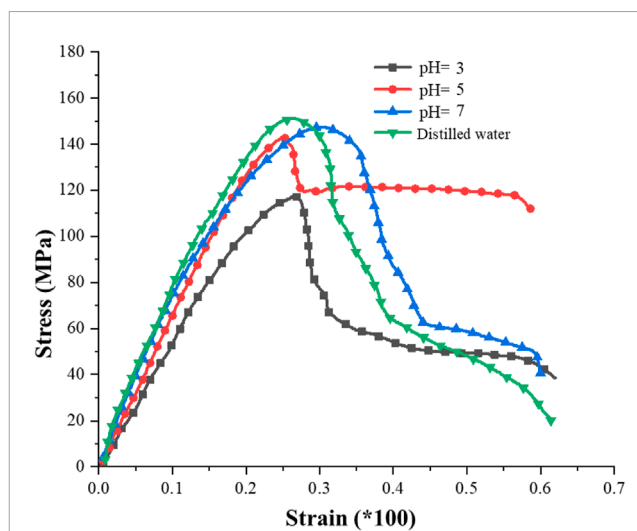

FIGURE 5
Stress-strain curves under uniaxial compression.

modulus of granite corroded by a solution with pH = 3 decreases by 18.24%–53.91 GPa. The elastic modulus serves as an indicator of the softening degree of the rock's deformation characteristics. As observed, with the decrease in the pH value of the corrosive solution, the slope of the stress-strain curve gradually decreases, and the elastic modulus of the corroded rock samples also decreases. In other words, the more acidic the corrosive solution (lower pH value), the smaller the elastic modulus of the corroded rock sample, indicating a more pronounced softening eect. Furthermore, the Poisson's ratio of granite exhibits significant sensitivity to the hydrochemical

FIGURE 6
Elastic modulus and Poisson's ratio of granite.
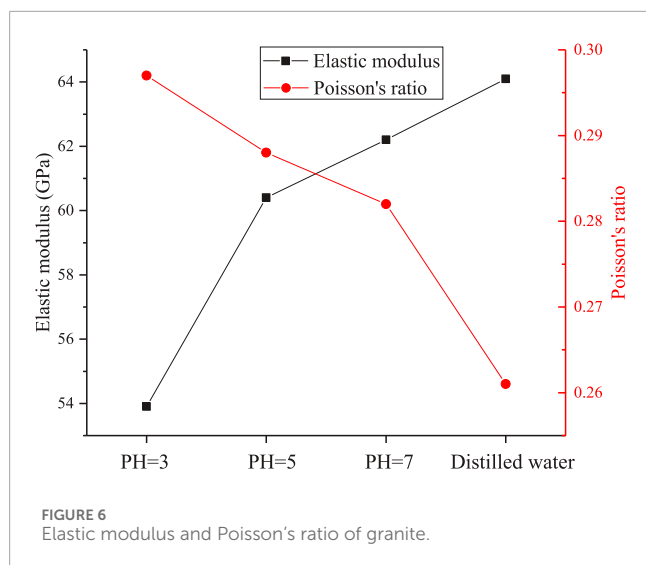
environment. After corrosion by solutions with dierent pH values, the Poisson's ratios of the granite increase, and the magnitude of this increase becomes larger as the pH value decreases. This suggests that the internal structure of the granite is altered by the chemical reactions with the corrosive solutions, leading to changes in its deformation behavior and mechanical properties.

4.2 Triaxial compression

The study employed confining pressures of 10 MPa, 20 MPa, and 30 MPa to investigate the eects on the mechanical and deformation properties of granite subjected to hydrochemical corrosion. Figure 7 presents the stress-strain curves of granite after hydrochemical corrosion under triaxial testing conditions. The presence of confining pressure significantly influences the mechanical and deformation behavior of granite, with dierent confining pressures corresponding to distinct mechanical parameters. It is evident that the distinction between the behavior of granite under dierent confining pressures becomes more pronounced after hydrochemical corrosion compared to naturally dried granite. Rocks corroded by solutions with varying pH values exhibit a decrease in their triaxial strength, with a more significant drop observed at lower pH values. Taking the example of a corrosive solution with pH = 3, after 60 days of corrosion, the peak strength decreases by 39.99% (at 10 MPa), 34.82% (at 20 MPa), and 30.61% (at 30 MPa), respectively. It is important to note that during the plastic yield stage, the confining pressure plays a crucial role in allowing suicient development and propagation of cracks within the rock. This results in a more pronounced yield stage on the stress-strain curve, with the yield phenomenon becoming more evident as the confining pressure increases. The confinement restricts the rapid failure of the rock by providing lateral support, allowing the internal cracks to grow and coalesce under increasing stress before ultimate failure occurs (Bi et al., 2016; Ren et al., 2023a; Ren et al., 2023b).

The internal friction angle and cohesion of granite are essential parameters for evaluating their mechanical properties. Based on the

triaxial stress-strain data of granite, an analysis can be conducted to investigate the trends in the changes of cohesion and internal friction angle after hydrochemical corrosion. Figure 8 illustrates the relationship between the peak strength of specimens and confining pressure after hydrochemical corrosion. It is evident from Figure 8 that, despite the eects of hydrochemical corrosion, the peak strength of the specimens maintains a good linear relationship with the confining pressure. This suggests that, although the rock's mechanical properties have been altered by the corrosion process, the fundamental relationship between peak strength and confining pressure remains intact.

The internal friction Angle and cohesion force can be calculated according to the Moore-Coulomb strength criterion, as shown below.

$$\varphi = \arcsin \frac{k-1}{k+1} \tag{2}$$

$$c = \frac{b(1 - \sin \varphi)}{2 \cos \varphi} \tag{3}$$

Where, c is the cohesion of the rock, φ is the internal friction angle of the rock, k is the slope of the line in the figure, and b is the intercept of the line in Figure 8.

Based on the experimental data presented in Figure 8, a linear regression analysis was conducted to discern trends in the changes of the internal friction angle and cohesion of granite subjected to various corrosive solutions. Subsequently, employing Equations 2, 3, the alterations in these mechanical properties were quantitatively determined. Figure 9 vividly illustrates the variation in both the internal friction angle and cohesion of granite after exposure to solutions with dierent pH values. Upon exposure to hydrochemical corrosion, a discernible decline was observed in both the cohesion and friction angle of the granite. (1) Specifically, regarding cohesion, after 60 days of corrosion by a solution with pH 5, the cohesion of the rock decreased from 32.24 MPa to 27.199 MPa, manifesting a decrease rate of 15.64%. Notably, when subjected to a more acidic solution with pH 3 for the same duration, the cohesion plummeted to 21.796 MPa, exhibiting a substantial attenuation rate of 32.39%. This underscores the pronounced sensitivity of rock cohesion to hydrochemical corrosion. (2) As for the internal friction angle, while it also decreased with the intensification of corrosion associated with lower pH values and corresponding greater degrees of rock damage, the magnitude of this change was markedly less pronounced than that observed in cohesion. Following 60 days of exposure to a pH 5 solution, the internal friction angle declined from its initial value of 51.96°–49.506°, reflecting a modest attenuation rate of 4.72%. Similarly, after 60 days in a pH 3 solution, the internal friction angle diminished to 48.7°, yielding a slightly higher attenuation rate of 6.27%. Collectively, these findings underscore the pivotal role of cohesion as an indicator of rock structural characteristics. Hydrochemical corrosion inflicts internal damage on granite, manifesting as the formation of microcracks and micropores, which in turn significantly alters their cohesion. Conversely, the internal friction angle, which serves as a metric of rock elastic properties, exhibits a lesser degree of sensitivity to such damage, though it does experience a measurable decrease.
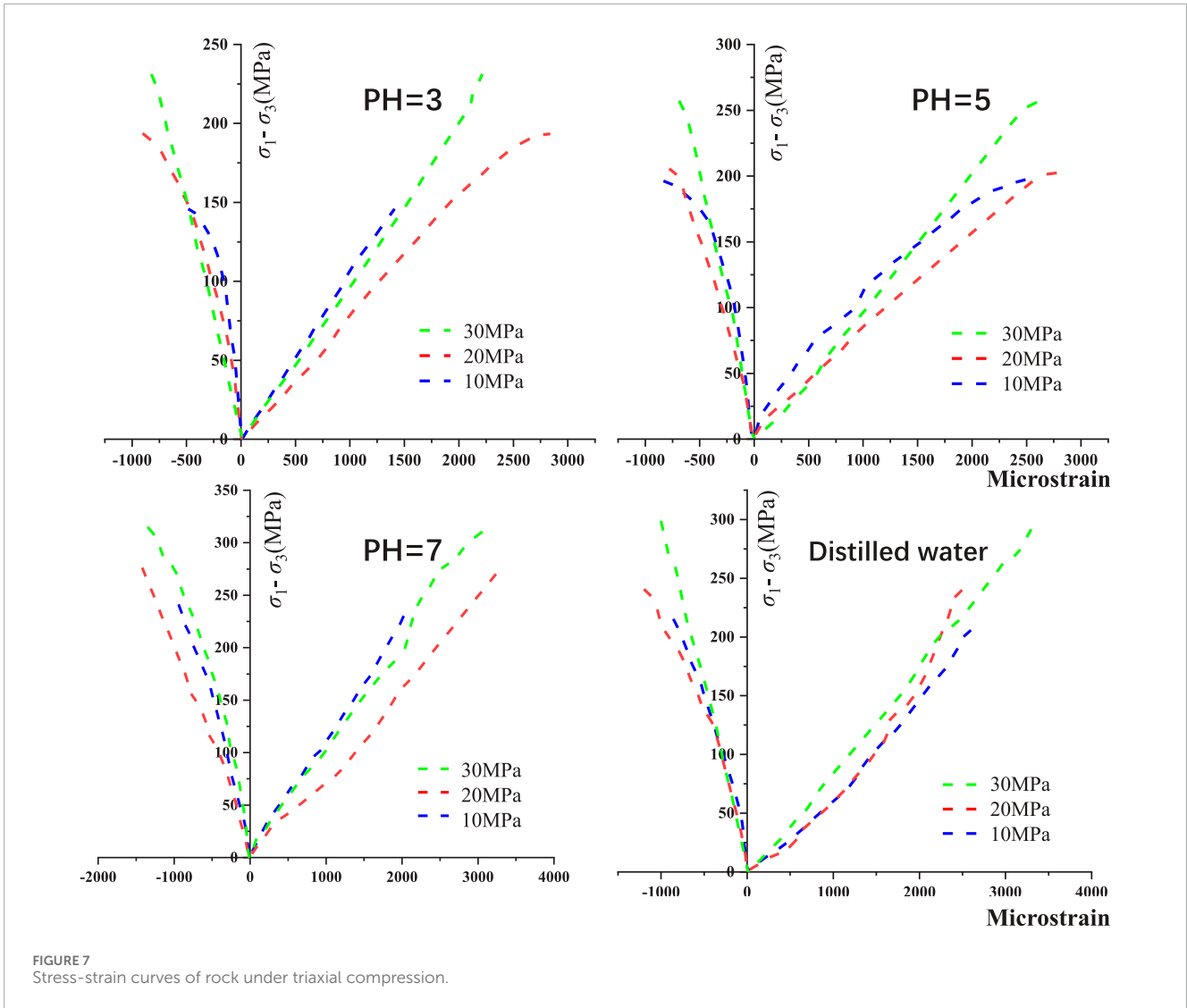
FIGURE 7
Stress-strain curves of rock under triaxial compression.

5 Energy evolution of rock after hydrochemical corrosion

5.1 Uniaxial compression

The internal mechanism of rock deformation and failure is essentially a process of interconversion among various forms of energy. When contemplating the essence of rock deformation and failure from an energetic perspective, one realizes that it is fundamentally characterized by the mutual transformation of energy in diverse forms. Throughout the process of rock failure, the primary energies involved are the total absorbed energy, elastic strain energy, and dissipated energy. Assuming that the rock is in an energetically isolated and closed environment during deformation, with no heat exchange occurring with the external surroundings, Equations 4–6: the following formulas can be derived based on the theory of energy dissipation and release (Qiao et al., 2022; Zhang et al., 2019b):
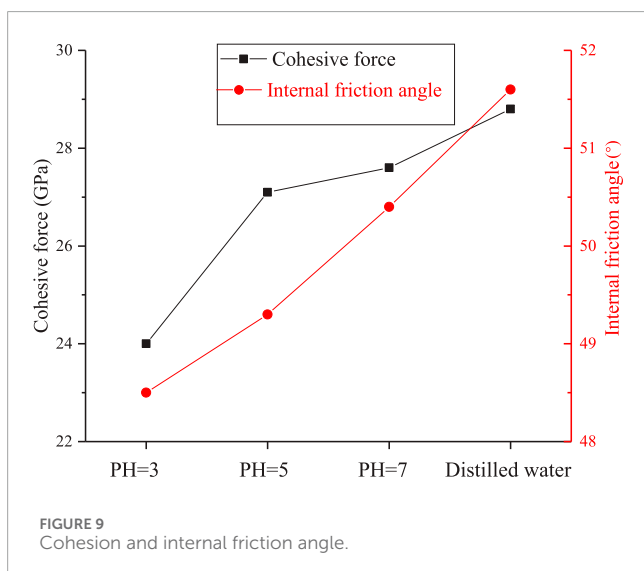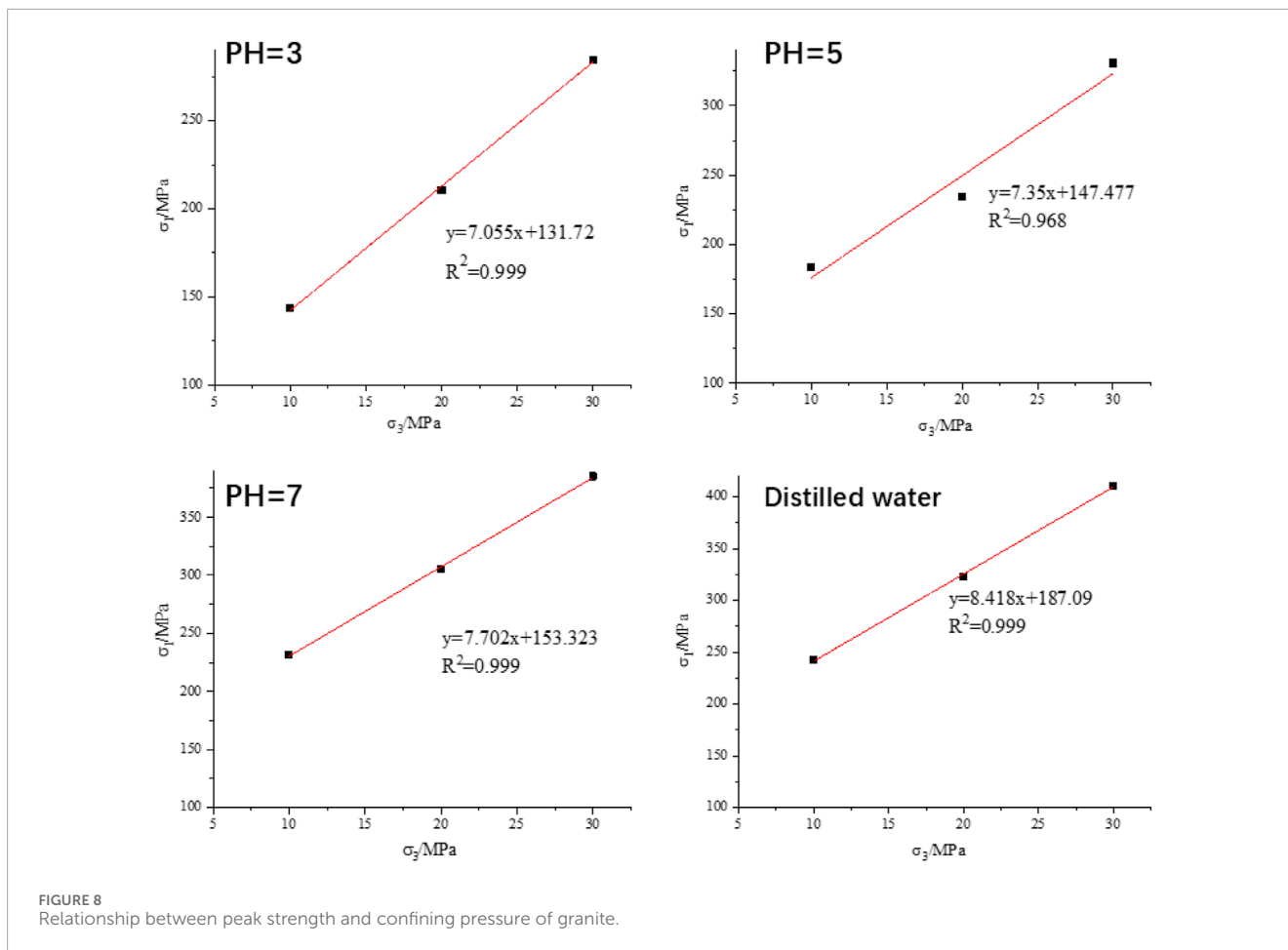
$$U^a = U^e + U^d \qquad (4)$$

$$U^a = \int_0^{\varepsilon_1} \sigma_1 d\varepsilon_1 + \int_0^{\varepsilon_2} \sigma_2 d\varepsilon_2 + \int_0^{\varepsilon_3} \sigma_3 d\varepsilon_3 \qquad (5)$$

$$U^e = \frac{1}{2}\left(\sigma_1 \varepsilon_1^e + \sigma_2 \varepsilon_2^e + \sigma_3 \varepsilon_3^e\right) = \frac{1}{2E_u}\left(\sigma_1^2 + \sigma_2^2 + \sigma_3^2\right) \qquad (6)$$

Where u^a is the total strain energy absorbed by the rock, u^e is the elastic strain energy accumulated inside the rock, and u^d is the dissipated strain energy driving micro-crack compaction and crack propagation. σ_1 and ε_1 are the axial stress and strain, ε_1^e is the elastic strain, and E_u is the unloading modulus. According to the results of other scholars (Qiao et al., 2022), E_u is approximately equal to the E.

Figure 10 illustrates the evolution of energy in granite subjected to corrosion by solutions with varying pH levels. It is evident that the three energy components of the granite exhibit a similar trend to the stress-strain curve. When the rock is treated with distilled water, during the elastic-plastic stage, the elastic energy exceeds the dissipated energy, indicating a strong energy storage capacity in the uncorroded rock. However, after corrosion with solutions of pH 5 and 7, the elastic energy in the rock is approximately equal to the dissipated energy during the elastic stage, signifying a

FIGURE 8
Relationship between peak strength and confining pressure of granite.

FIGURE 9
Cohesion and internal friction angle.

propagate further during mechanical testing, thereby reducing the rock's energy storage characteristics.

Figure 11 depicts the relationship between each energy component and strain in granite. At the same strain level, the total energy of the rock decreases as the pH value decreases. For pH values of 5 and 7, the elastic energy prior to peak stress is comparable. However, when the pH drops to 3, there is a notable decrease in the elastic energy of the rock. Prior to peak stress, the dissipated energy curves are similar for all conditions, except for pH 5, where a distinct yield plateau is observed post-peak stress, resulting in significantly higher dissipated energy compared to the other groups.

5.2 Triaxial compression

Figures 12–14 showcase the evolution of the three energy components in granite under varying confining pressures. As the confining pressure increases, all energy values exhibit a significant rise. When the pH is 3, the three energy components of the rock are at their minimum, indicating the highest degree of damage within the rock. Intriguingly, at lower confining pressures, the energy curves within each group exhibit more pronounced dierences. However, as the confining pressure increases, the energy curves tend to converge, suggesting that under high confining pressures, the internal cracks within the rock are eectively closed,

weakened energy storage capability. At a pH of 3, the elastic energy is lower than the dissipated energy throughout the elastic-plastic stage, revealing the weakest energy storage capacity among the tested conditions. This suggests that at the lowest pH, the solution induces the formation of additional cracks within the rock, which tend to
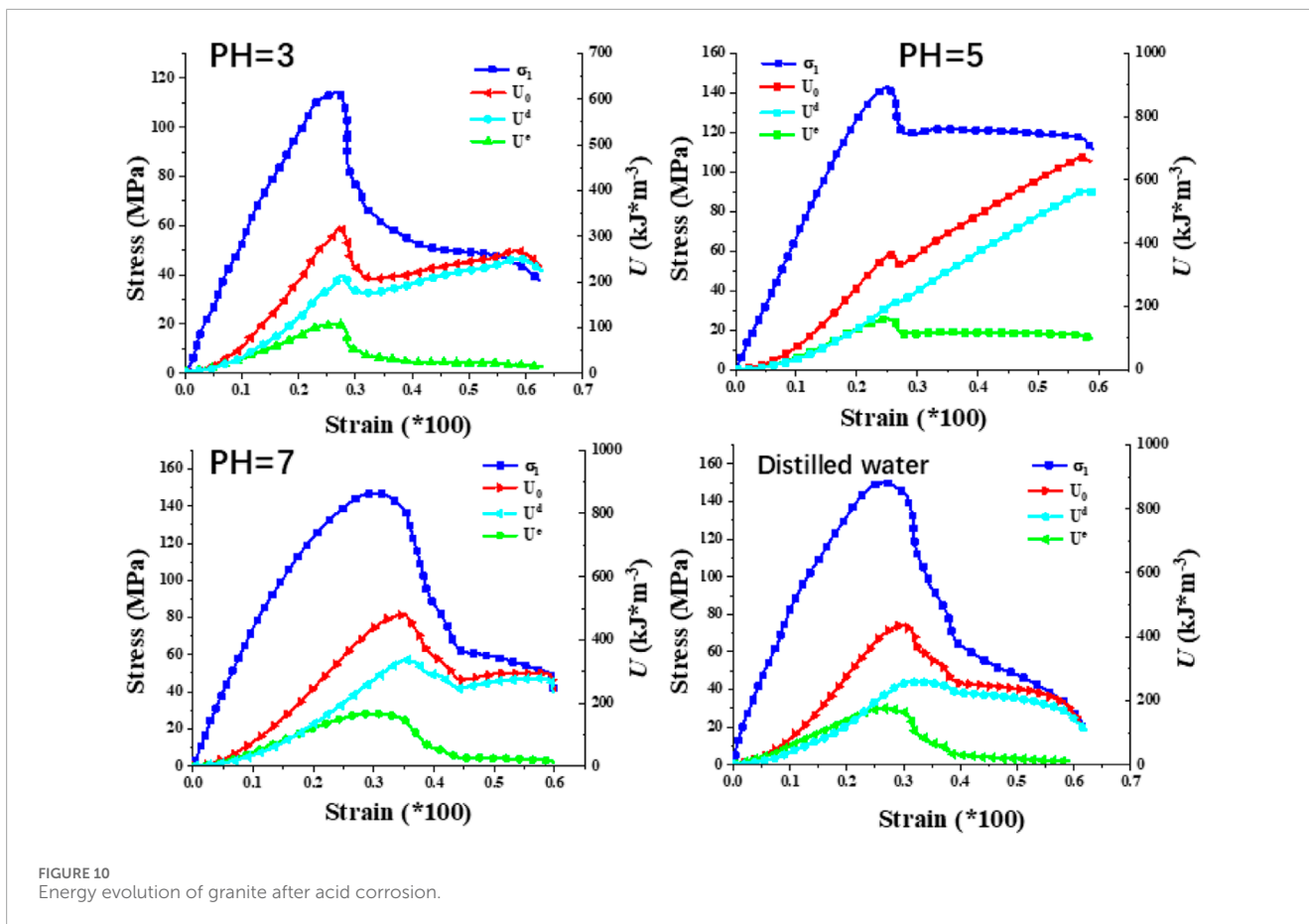
FIGURE 10
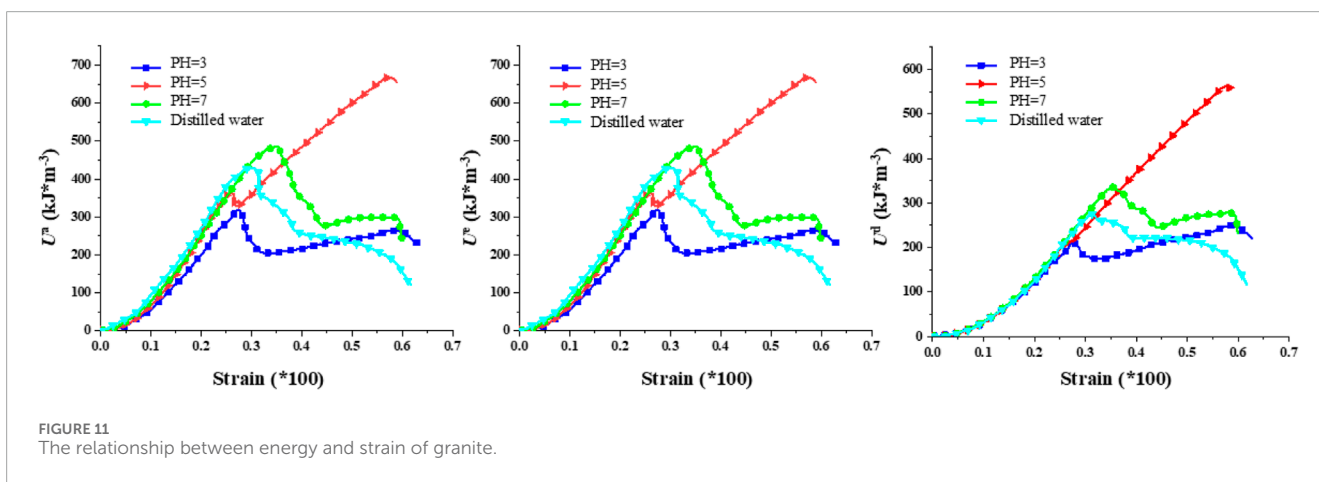Energy evolution of granite after acid corrosion.

FIGURE 11
The relationship between energy and strain of granite.

resulting in comparable energy values for the three components. This phenomenon implies that among the factors influencing the energy values of granite, the confining pressure appears to have a higher priority than the pH value. This observation underscores the importance of confining pressure in modulating the mechanical behavior and energy storage capacity of granite, particularly in environments where granite is subjected to both chemical corrosion and mechanical stress. The ability of high confining pressures to mitigate the eects of chemical corrosion on rock properties highlights the complex interplay between physical and chemical

processes that govern the stability and performance of granite in natural and engineered systems.

To profoundly characterize the influence of hydrochemical solutions on the three energy magnitudes of granite, Figure 15 illustrates the ultimate values of these energies under varying confining pressures. (1) Regarding the maximum total energy, under the corrosion of chemical solutions with the same pH value, a higher confining pressure allows for a greater input of mechanical energy. Additionally, at a constant confining pressure, the total energy exhibits an upward trend with an increase in pH value. For instance,
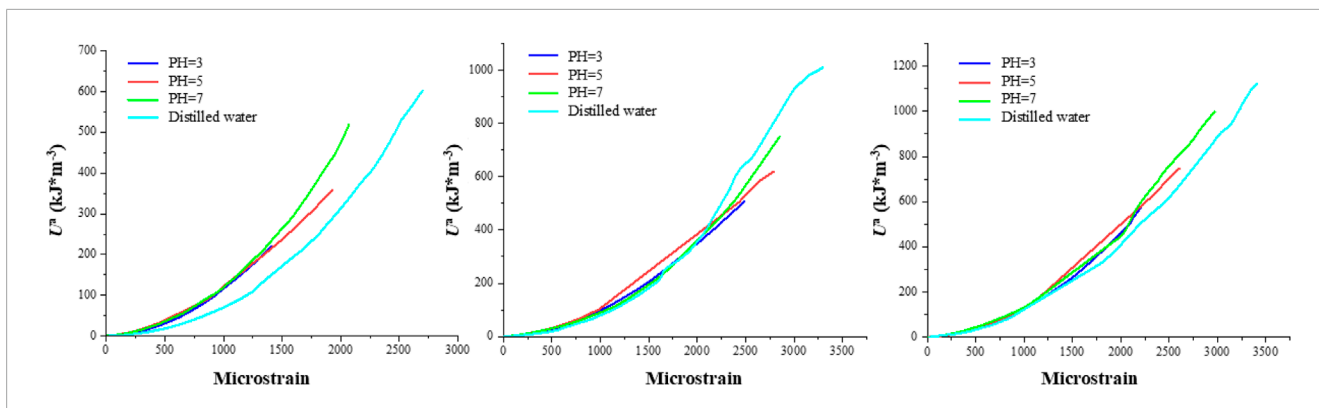
FIGURE 12
Changes in total input energy (10 MPa, 20 MPa and 30 MPa from left to right).
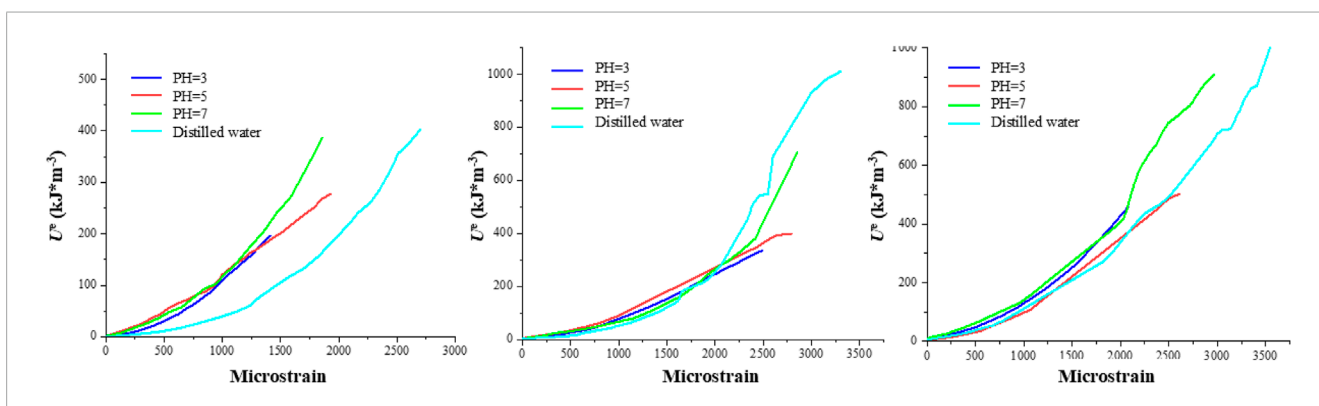
FIGURE 13
Changes in elastic strain energy (10 MPa, 20 MPa and 30 MPa from left to right).
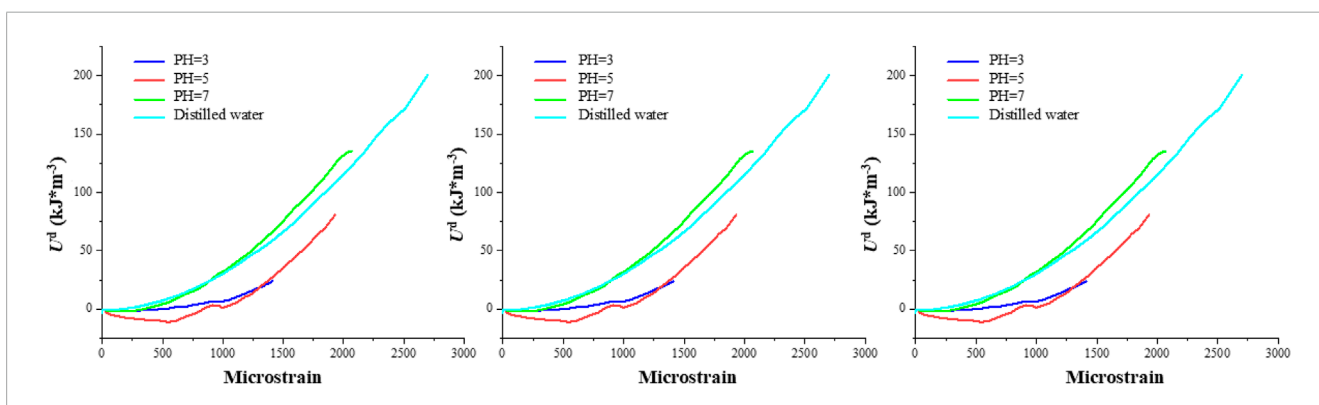
FIGURE 14
Changes in dissipated strain energy (10 MPa, 20 MPa and 30 MPa from left to right).

at a confining pressure of 10 MPa, the maximum total input energies are 155.98 kJ/m³, 358.19 kJ/m³, 518.56 kJ/m³, and 601.96 kJ/m³, respectively. Conversely, at a confining pressure of 20 MPa, the maximum total input energies rise to 508.02 kJ/m³, 620.17 kJ/m³, 750.03 kJ/m³, and 1,010.37 kJ/m³, respectively. (2) With respect to the elastic energy storage limit, under the corrosion of chemical solutions with identical pH values, a higher confining pressure correlates with a higher elastic energy of the specimen. Similarly, at

a fixed confining pressure, the elastic energy displays an ascending trend as the pH value increases. For example, at a confining pressure of 10 MPa, the elastic energy limits are 196.03 kJ/m³, 277.48 kJ/m³, 386.36 kJ/m³, and 401.22 kJ/m³, respectively. In contrast, at a confining pressure of 20 MPa, these limits escalate to 335.23 kJ/m³, 398.36 kJ/m³, 703.11 kJ/m³, and 980.69 kJ/m³, respectively. (3) Regarding the dissipation energy limit, at lower confining pressures, the energy exhibits a linear increase. However, at higher confining

FIGURE 15
Relation between energy and PH value under dierent confining pressures.
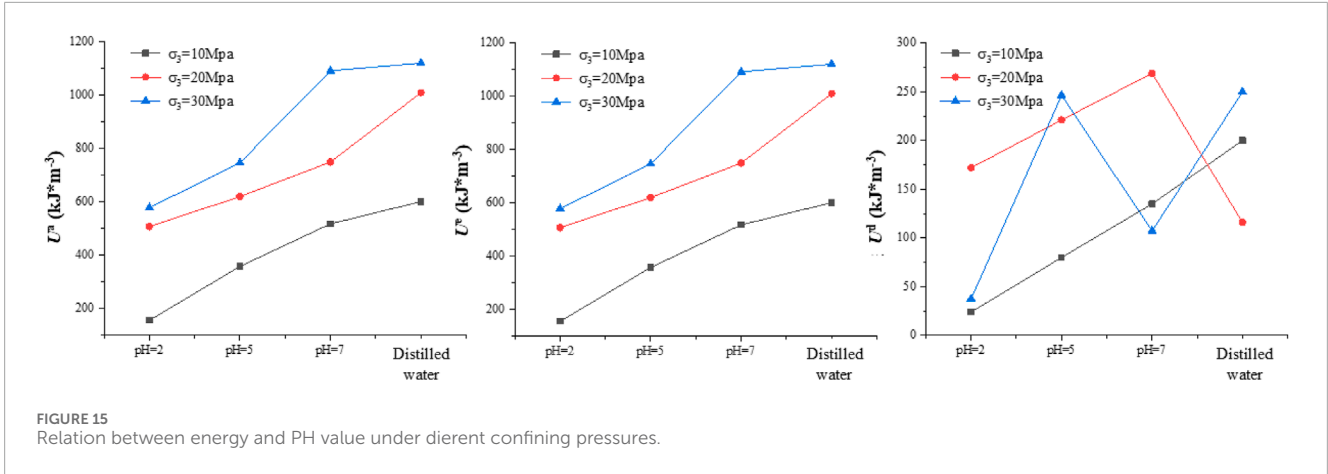
pressures, the dissipation energy displays a degree of variability, which is attributed to the disordered nature of the post-peak stress-strain curve.

6 Comprehensive evaluation system for chemical corrosion

The comprehensive evaluation of hydrochemical corrosion involves considering multiple parameters of the corroded rock as influencing factors and assigning dierent weights to each, thereby enabling a quantitative assessment of the hydrochemical corrosion process. In the process of assigning weights, it is crucial to minimize the influence of subjective scoring while evaluating the independence among the various influencing factors. This paper adopts the CRITIC (Criteria Importance Through Intercriteria Correlation) weighting method (Parisi et al., 2019; Akram et al., 2024) to construct a comprehensive evaluation system for the hydrochemical corrosion process. A matrix $X = (x_{ij})a*b$ can be constructed if there are a object to be evaluated and b evaluation indicators of influencing factors, and the element after indicator forward processing is x'_{ij}.

Equations 7–13: For data with smaller indicators and better results (Parisi et al., 2019; Akram et al., 2024):

$$x'_{ij} = \frac{\max(x_j) - x_{ij}}{\max(x_j) - \min(x_j)} \tag{7}$$

For data with larger indicators and better results:

$$x'_{ij} = \frac{x_{ij} - \min(x_j)}{\max(x_j) - \min(x_j)} \tag{8}$$

When determining the weights of influencing factors using the CRITIC weighting method, two fundamental concepts are primarily considered. Firstly, contrast, which refers to the extent of variation within each influencing factor, is typically measured by the standard deviation of its values. A larger standard deviation signifies greater volatility within the factor, thereby justifying a higher weight. Secondly, conflict, which pertains to the correlation between dierent influencing factors, is evaluated. A lower degree of correlation

indicates greater independence between factors, resulting in a higher weight being assigned (Parisi et al., 2019; Akram et al., 2024).

$$\begin{cases} \sigma_j = \sqrt{\dfrac{\sum_{i=1}^{a}\left(x'_{ij} - \overline{x'}_j\right)}{a - 1}} \\ f_j = \sum_{i=1}^{a}\left(1 - r_{ij}\right) \end{cases} \tag{9}$$

where q represents the correlation coeicient between indicator i and indicator j.

The Pearson coeicient is used here and is calculated as follows.

$$r_{ij} = \frac{\sum_{i=1}^{a}\left(x_i - \overline{X}\right)\left(y_i - \overline{Y}\right)}{\sqrt{\sum_{i=1}^{a}\left(x_i - \overline{X}\right)^2}\sqrt{\sum_{i=1}^{a}\left(y_i - \overline{Y}\right)^2}} \tag{10}$$

Therefore, the amount of information in each data is:

$$C_j = \sigma_j \sum_{i=1}^{a}\left(1 - r_{ij}\right) = \sigma_j \times f_j \tag{11}$$

The calculated weight of this data is:

$$\omega_j = \frac{C_j}{\sum_{j=1}^{b} C_j} \tag{12}$$

The calculated score for this data is:

$$S_j = \sum_{j=1}^{n} \omega_j x'_{ij} \tag{13}$$

According to the above theory, rock samples under dierent corrosion environments were taken as examples to evaluate their hydrochemical corrosion conditions, and Matlab software was used to process the data. Table 2 shows the normalized rock physical and mechanical parameters.

The contrast and contradiction between the calculated data provide a basis for assigning weight to a certain group of data. The calculated results are shown in Table 3.

Calculate the information load of the data, and assign weight to the final value of the factor. The information load calculation results and the weight are shown in Table 4.

Based on the comprehensive evaluation of hydrochemical corrosion for various rock types under dierent corrosive

TABLE 2 Physical and mechanical parameters of granite (standardized).

Sample	Wave velocity (m/s)	Uniaxial compressive strength (MPa)	Triaxial compressive strength (MPa)
PH3-1	1.0000	1.0000	1.0000
PH3-2	0.8813	0.9549	0.9647
PH3-3	0.7121	0.9788	0.9722
PH5-1	0.8424	0.3289	0.5507
PH5-2	0.6420	0.3767	0.5258
PH5-3	0.5292	0.3714	0.5553
PH7-1	0.3444	0.0000	0.0194
PH7-2	0.0282	0.0212	0.0261
PH7-3	0.0000	0.0265	0.0000

TABLE 3 Data contrast and contradiction of dierent influencing factors.

Sample	Wave velocity (m/s)	Uniaxial compressive strength (MPa)	Triaxial compressive strength (MPa)
Contrast	0.3623	0.4226	0.4182
contradiction	0.6509	0.3577	0.2140

TABLE 4 Data information load and weighting results.

Sample	Wave velocity (m/s)	Uniaxial compressive strength (MPa)	Triaxial compressive strength (MPa)
Information load	0.2358	0.1512	0.0895
Weight	0.2619	0.1679	0.0994

environments, as depicted in Figure 16, it is evident that the scores of the granite gradually decrease as the pH value of the solution decreases. This observation aligns with the previous discussion, reinforcing the notion that acidic solutions significantly alter the internal structure of granite. Specifically, the decrease in scores with decreasing pH indicates an increase in the severity of corrosion eects on the granite. The acidic environment promotes chemical reactions that break down the mineral components of the granite, leading to structural degradation and weakening of the rock matrix. This process can manifest as dissolution of minerals, formation of cracks and pores, and overall loss of integrity and strength.

Therefore, the results presented in Figure 16 not only validate the theoretical understanding of the corrosive eects of acidic solutions on granite but also provide empirical evidence of the detrimental impact of such environments on the durability and stability of rock formations. The analysis underscores the importance of considering the pH of the surrounding environment when assessing the potential for hydrochemical corrosion and designing mitigation strategies to protect rock structures from degradation.

FIGURE 16
Comprehensive score of granite after corrosion.
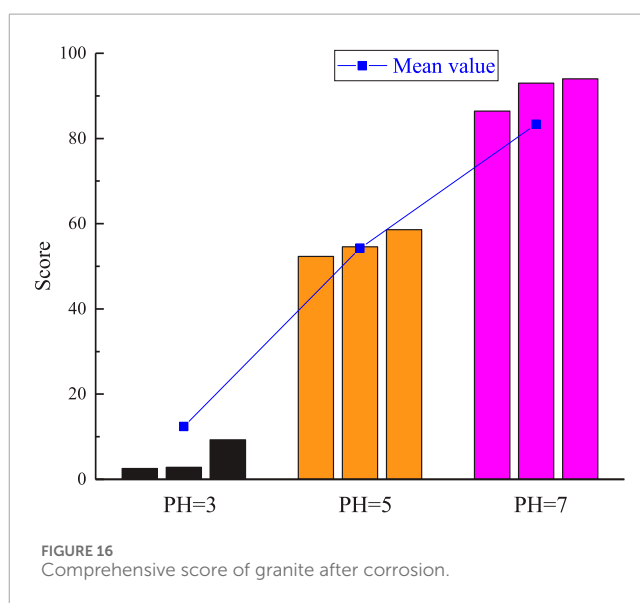
7 Conclusion

This study meticulously examines the macroscopic and microscopic morphologies of granite subjected to various corrosive solutions, along with the alterations in various physical and mechanical parameters. Utilizing the weighting methodology, a scientific and comprehensive evaluation system for the post-hydrochemical corrosion of deep rock has been established. The detailed conclusions are as follows.

(1) The mineral constituents of granite can undergo chemical reactions with H^+ ions present in acidic saline solutions, leading to the formation of minute interconnected regions within the rock matrix. This results in a rough macroscopic appearance. The lower the pH value of the solution, the more pronounced the corrosion traces become in both the microscopic and macroscopic morphologies of the sample, and the maximum wave velocity is reduced by 13.46%.

(2) When the solution reaches its lowest (pH=3), granite exhibits a distinct post-peak yield stage while still retaining a certain level of load-bearing capacity. With further decreases in solution pH, the elastic modulus of the rock gradually diminishes (from 64.10 GPa to 53.91 GPa), while the Poisson's ratio gradually increases (from 0.26 to 0.30). Concurrently, both the cohesion and internal friction angle of granite decrease synchronously as the pH value drops.

(3) When the pH=3, the solution induces the formation of more cracks within the rock, significantly weakening its energy storage characteristics. As the pH value decreases, both the total absorbed energy limit and the elastic strain energy limit of the granite system decrease markedly.

(4) This study employs the CRITIC weighting method, which comprehensively considers the contrast and conflict among parameters, to construct a comprehensive evaluation system for deep granite subjected to hydrochemical corrosion. This system provides valuable reference for investigating the damage patterns of granite in acid-base corrosion engineering projects.

Data availability statement

The raw data supporting the conclusions of this article will be made available by the authors, without undue reservation.

Author contributions

JZ: Methodology, Supervision, Conceptualization, Formal analysis, Investigation, Visualization, Software, Writing–review and editing. BZ: Conceptualization, Methodology, Validation, Writing–original draft, Writing–review and editing. YS: Project administration, Software, Supervision, Validation, Writing–review and editing. TY: Data curation, Project administration, Validation, Writing–original draft.

Funding

Conflict of interest

The authors declare that the research was conducted in the absence of any commercial or financial relationships that could be construed as a potential conflict of interest.

Publisher's note

All claims expressed in this article are solely those of the authors and do not necessarily represent those of their affiliated organizations, or those of the publisher, the editors and the reviewers. Any product that may be evaluated in this article, or claim that may be made by its manufacturer, is not guaranteed or endorsed by the publisher.

References

Akram, M., Zahid, S., and Deveci, M. (2024). Enhanced CRITIC-REGIME method for decision making based on Pythagorean fuzzy rough number. *Expert Syst. Appl.* 238, 122014. doi:10.1016/j.eswa.2023.122014

Anderson, O. L., and Grew, P. C. (1977). Stress corrosion theory of crack propagation with applications to geophysics. *Rev. Geophys.* 15 (1), 77–104. doi:10.1029/rg015i001p00077

Atkinson, B. K., and Meredith, P. G. (1981). Stress corrosion cracking of quartz: a note on the influence of chemical environment. *Tectonophysics* 77 (1/2), 1–11. doi:10.1016/0040-1951(81)90157-8

Bi, J., Zhou, X. P., and Qian, Q. H. (2016). The 3D numerical simulation for the propagation process of multiple pre-existing flaws in rock-like materials subjected to biaxial compressive loads. *Rock Mech. Rock Eng.* 49 (5), 1611–1627. doi:10.1007/s00603-015-0867-y

Ceglia, F., Macaluso, A., Marrasso, E., Sasso, M., and Vanoli, L. (2020). Modelling of polymeric shell and tube heat exchangers for low-medium temperature geothermal applications. *Energies* 13 (11), 2737. doi:10.3390/en13112737

Chen, L., Jia, B., and Zhang, S. (2022). Study on mechanical behavior and energy mechanism of sandstone under chemical corrosion. *Materials* 15 (4), 1613. doi:10.3390/ma15041613

Chen, W., Liu, J., Peng, W., Zhao, Y., Luo, S., Wan, W., et al. (2023). Aging deterioration of mechanical properties on coal-rock combinations considering hydro-chemical corrosion. *Energy* 282, 128770. doi:10.1016/j.energy.2023.128770

Deng, Y., Meng, L., Zhang, M., Li, L., Yao, Z., and Zhao, H. (2024). Sulfate corrosion resistance of reclaimed coal gangue sand concrete reinforced with silica fume. *Iran. J. Sci. Technology-Transactions Civ. Eng.* doi:10.1007/s40996-024-01392-y

Fang, W. W., Li, M. X., Huang, P., Shi, T., Chen, Y., et al. (2024). Study on failure mechanism and control of surrounding rock of inclined strata crossing roadway in deep coal mine. *Front. Earth Sci.* 12, 1378264. doi:10.3389/feart.2024.1338670

Fang, X., Xu, J., and Wang, P. (2018). Compressive failure characteristics of yellow sandstone subjected to the coupling eects of chemical corrosion and repeated freezing and thawing. *Eng. Geol.* 233, 160–171. doi:10.1016/j.enggeo.2017.12.014

Fu, Q., Yang, J., Gao, Y. B., Song, H., Liu, Y., et al. (2024). Combined blasting for protection of gob-side roadway with thick and hard roof. *J. Rock Mech. Geotechnical Eng.* 16 (8), 3165–3180. doi:10.1016/j.jrmge.2023.11.027

Gong, C., Wang, W., Shao, J., Wang, R. B., and Feng, X. W. (2021). Eect of water chemical corrosion on mechanical properties and failure modes of pre-fissured sandstone under uniaxial compression. *Acta Geotech.* 16 (4), 1083–1099. doi:10.1007/s11440-020-01071-y

Hao, J. W., Qiao, L., and Li, Q. W. (2022b). Study on cross-scale pores fractal characteristics of granite after high temperature and rock failure precursor under uniaxial compression. *Powder Technol.* 401, 117330. doi:10.1016/j.powtec.2022.117330

Hao, J. W., Qiao, L., Liu, Z. Y., and Li, Q. (2022a). Eect of thermal treatment on physical and mechanical properties of sandstone for thermal energy storage: a comprehensive experimental study. *Acta Geotech.* 17 (9), 3887–3908. doi:10.1007/s11440-022-01514-8

Lin, Y., Zhou, K., Gao, F., Liu, T., and Liu, C. (2019). Experimental investigations on pore structure and mechanical properties of sandstone subjected to chemical corrosion. *IEEE Access* 7, 116706–116721. doi:10.1109/access.2019.2932421

Pan, J., Ma, Y., Zhang, L., Ning, Z., and Xi, X. (2024). Eect of chemical corrosion on rock fracture behavior in coastal deep mines: insights from mechanical and acoustic characteristics. *J. Mar. Sci. Eng.* 12 (6), 869. doi:10.3390/jmse12060869

Parisi, S., Tangkaratt, V., Peters, J., and Khan, M. E. (2019). TD-regularized actor-critic methods. *Mach. Learn.* 108 (8-9), 1467–1501. doi:10.1007/s10994-019-05788-0

Qiao, L., Hao, J., Liu, Z., Li, Q., and Deng, N. (2022). Influence of temperature on the transformation and self-control of energy during sandstone damage: experimental and theoretical research. *Int. J. Min. Sci. Technol.* 32 (4), 761–777. doi:10.1016/j.ijmst.2022.02.008

Ren, F. Q., Zhu, C., He, M. C., Shang, J., Feng, G., and Bai, J. (2023a). Characteristics and precursor of static and dynamic triggered rockburst: insight from multifractal. *Rock Mech. Rock Eng.* 56 (3), 1945–1967. doi:10.1007/s00603-022-03173-3

Ren, F. Q., Zhu, C., Karakus, M., and He, M. (2024). Rockburst mitigation mechanisms of pressure relief borehole and rock bolt support: insights from granite true triaxial unloading rockburst tests. *Eng. Geol.* 336, 107571. doi:10.1016/j.enggeo.2024.107571

Ren, F. Q., Zhu, C., Yuan, Z. H., Karakus, M., Tang, S., and He, M. (2023b). Recognition of shear and tension signals based on acoustic emission parameters and waveform using machine learning methods. *Int. J. Rock Mech. Min. Sci.* 171, 105578. doi:10.1016/j.ijrmms.2023.105578

Wang, W., Mei, S., Cao, Y., Wang, R., and Zhu, Q. (2023). Experimental study on property modification of jointed rocks subjected to chemical corrosion. *Eur. J. Environ. Civ. Eng.* 27 (6), 2313–2324. doi:10.1080/19648189.2020.1752808

Wang, Y. T., Zhou, X. P., Wang, Y., and Shou, Y. (2018). A 3-D conjugated bond-pair-based peridynamic formulation for initiation and propagation of cracks in brittle solids. *Int. J. Solids Struct.* 134, 89–115. doi:10.1016/j.ijsolstr.2017.10.022

Wang, Y. T., Zhou, X. P., and Xu, X. (2016). Numerical simulation of propagation and coalescence of flaws in rock materials under compressive loads using the extended non-ordinary state-based peridynamics. *Eng. Fract. Mech.* 163, 248–273. doi:10.1016/j.engfracmech.2016.06.013

Wu, Y., Dong, Q., and He, J. (2021). The eect of chemical corrosion on mechanics and failure behaviour of limestone containing a single kinked fissure. *Sensors* 21 (16), 5641. doi:10.3390/s21165641

Xue, J., Zhao, Z., Dong, L., Jin, J., Zhang, Y., Tan, L., et al. (2022). Eect of chemical corrosion and axial compression on the dynamic strength degradation characteristics of white sandstone under cyclic impact. *Minerals* 12 (4), 429. doi:10.3390/min12040429

Yang, X., Jiang, A., and Li, M. (2019). Experimental investigation of the time-dependent behavior of quartz sandstone and quartzite under the combined eects of chemical erosion and freeze-thaw cycles. *Cold Regions Sci. Technol.* 161, 51–62. doi:10.1016/j.coldregions.2019.03.008

Zhang, J. Z., Zhou, X. P., Zhou, L. S., and Berto, F. (2019a). Progressive failure of brittle rocks with non-isometric flaws: insights from acousto-optic-mechanical (AOM) data. *Fatigue and Fract. Eng. Mater. and Struct.* 42 (8), 1787–1802. doi:10.1111/e.13019

Zhang, Y., Feng, X. T., Zhang, X. W., Wang, Z. F., and Sharifzadeh, M. (2019b). Strain energy evolution characteristics and mechanisms of hard rocks under true triaxial compression. *Eng. Geol.* 260: 105222. doi:10.1016/j.enggeo.2019.105222

Zhao, J. S., Zhang, J. C., Pei, S. F., Xing, L., Chen, C. F., and Zhang, G. D. (2024). Investigation on the failure mechanism of the collapse of the columnar jointed basalt in underground cavern. *Front. Earth Sci.* 12, 1378264. doi:10.3389/feart.2024.1378264

Zhao, Y., Bi, J., Wang, C. L., and Liu, P. (2021). Eect of unloading rate on the mechanical behavior and fracture characteristics of sandstones under complex triaxial stress conditions. *Rock Mech. Rock Eng.* 54 (9), 4851–4866. doi:10.1007/s00603-021-02515-x

Zhao, Y., Wang, C. L., and Bi, J. (2020). Analysis of fractured rock permeability evolution under unloading conditions by the model of elastoplastic contact between rough surfaces. *Rock Mech. Rock Eng.* 53 (12), 5795–5808. doi:10.1007/s00603-020-02224-x

Zhou, X., and Yu, T. (2022). Experimental study on the dynamic failure behaviors of granite after chemical corrosion. *Rock Mech. Rock Eng.* 12 (4), 429. doi:10.1007/s00603-023-03506-w

Zhou, X. P., Wang, Y. T., Zhang, J. Z., and Liu, F. N. (2019). Fracturing behavior study of three-flawed specimens by uniaxial compression and 3D digital image correlation: sensitivity to brittleness. *Rock Mech. Rock Eng.* 52 (3), 691–718. doi:10.1007/s00603-018-1600-4